applied sciences

MDPI

Article

Surface Mechanical Properties of Acid-Etched Siliceous Limestone Fractures Under Deep, High-Temperature Conditions

Ze Li [1,2], Jian Yang [1,2], Huan Peng [1,2,3], Yuntao Liu [1,2], Xu Liu [1,2], Ruoyu Yang [1,2], Yucheng Jia [1] and Yajun Cao [4,5,*]

[1] Oil and Gas Technology Research Institute, PetroChina Southwest Oil and Gas Field Company, Chengdu 610017, China; lize9478@163.com (Z.L.); yj08@petrochina.com.cn (J.Y.); peng_huan@petrochina.com.cn (H.P.)
[2] Exploration Division, PetroChina Southwest Oil and Gas Field Company, Chengdu 621000, China
[3] Faculty of Elite Engineers, China University of Geosciences, Wuhan 430074, China
[4] Key Laboratory of Geomechanics and Embankment Engineering of the Ministry of Education, Hohai University, Nanjing 210098, China
[5] Institute of Geotechnical Engineering, Hohai University, Nanjing 210098, China
* Correspondence: caoyajun@hhu.edu.cn

Abstract

Acid etching alters both the geometry and the near-surface mechanical properties of carbonate fracture surfaces, yet surface morphology alone may not reliably indicate mechanical weakening. This study investigated siliceous limestone through rock-slab acid-etching tests at 140 °C, three-dimensional laser scanning, and nanoindentation within calcite grains, comparing gelled acid, a premixed self-generating-acid/gelled-acid system, and integrated variable-viscosity (IVV) acid under different injection conditions. Surface roughness, fractal dimension, and directional tortuosity were evaluated alongside elastic modulus, hardness, and indentation-derived fracture toughness, and a comprehensive damage index was introduced to couple etching depth with mechanical-property loss. The results show that low macroscopic roughness can coexist with substantial local mechanical weakening: the comparatively smooth surface obtained with gelled acid at 20 mL/min still exhibited a reduction of nearly 90% in calcite-grain hardness. Among the morphological parameters examined, fractal dimension showed the strongest association with the measured mechanical parameters, most notably with hardness. These findings support joint morphological and micromechanical characterization of acid-etched fracture surfaces and caution against assessing acid-etching quality from surface roughness alone.

Keywords: siliceous limestone; acid-etched fracture; surface mechanical properties; damage

Check for updates

Academic Editor: Ricardo Castedo Ruiz

Received: 17 September 2026
Revised: 22 October 2026
Accepted: 23 October 2026
Published: 27 October 2026

Copyright: © 2026 by the authors. Licensee MDPI, Basel, Switzerland. This article is an open access article distributed under the terms and conditions of the Creative Commons Attribution (CC BY) license.

1. Introduction

Carbonate reservoirs remain important targets for oil and gas development, and acid fracturing is widely used where matrix permeability is low. The treatment relies on a simple idea: acid removes rock unevenly along a hydraulic fracture, leaving asperities and channels that keep the fracture conductive after pumping stops. Deep reservoirs make this harder to achieve. High temperature accelerates acid–rock reactions and limits the distance reached by live acid, whereas high closure stress promotes asperity deformation and progressive fracture closure [1–4]. The quality of the etched surface, rather than dissolution alone, therefore controls whether conductivity can be sustained.

Where the rock is removed matters as much as how much is removed. Three-dimensional measurements have identified uniform, pitted, rough, and channelized etching patterns, each with a different response to closure stress [5–7]. Their development depends

on the initial fracture topography, mineral distribution, acid formulation, injection rate, and contact time. Siliceous limestone is a distinctive lithology widely distributed in deep carbonate reservoirs and consists mainly of calcite and quartz. Calcite readily dissolves in acid, whereas quartz is chemically stable and nearly insoluble. This mineralogical heterogeneity gives rise to pronounced differential dissolution during acid etching [8].

To date, most studies of acid-etched fractures have focused on surface geometry or fracture conductivity [9,10]. The mechanical condition of the etched surface has received less attention. Acid can dissolve mineral grains and intergranular cement, open pores and microcracks, and reduce the strength and elastic modulus of carbonate rock [11,12]. Scratch tests further show that surface strength is spatially variable and evolves with mineral composition and acid-contact time [13]. This point is important under reservoir stress: weakened asperities may deform, crush, or shear even when the post-etching topography initially appears favourable. However, the trade-off between dissolution and mechanical damage is still not well constrained.

Nanoindentation offers a direct way to examine that trade-off. Elastic modulus and hardness can be obtained from load–displacement curves using the method of Oliver and Pharr [14], while mineral-scale measurements can be linked to local composition through SEM-EDS or related imaging methods [15]. Even so, few studies have applied nanoindentation directly to acid-etched siliceous limestone fracture surfaces under conditions representative of deep, high-temperature reservoirs. Work on relatively pure limestone or dolomite does not fully capture the contrasting behaviour of calcite and quartz. The connection between visible etching morphology and local mechanical degradation therefore remains uncertain.

Acid-etched fracture surfaces with favourable, smooth macroscopic morphology may still suffer severe near-surface mechanical degradation, which cannot be inferred solely from conventional morphological characterization. To address this gap, the present study combines rock-slab acid-etching tests at 140 °C, three-dimensional laser scanning, and nanoindentation. Gelled acid, a premixed self-generating-acid/gelled-acid system, and an integrated variable-viscosity acid are compared under different injection conditions. Surface morphology is quantified using arithmetic mean roughness, fractal dimension, and directional tortuosity, and the changes in elastic modulus, hardness, and fracture toughness are measured at the same scale. A comprehensive damage index is then used to couple etching depth with mechanical-property loss. This work aims to determine how acid formulation and operating parameters shape both the geometry and the load-bearing capacity of siliceous limestone fracture surfaces, to provide insights into potential risks for long-term fracture conductivity.

2. Experimental Program

2.1. Rock Specimen Preparation

The test material was siliceous limestone obtained from a deep carbonate reservoir. Field cores were machined into the specimens shown in Figure 1. Each slab conformed to the standard API geometry and measured 178 mm long, 38 mm wide, and 25 mm thick. The flatness error of both end faces was kept within 0.05 mm. Whole-slide scanning showed that the siliceous limestone consisted mainly of calcite (approximately 70–80%) and quartz (approximately 15–25%), with a small amount of clay minerals. The XRD pattern in Figure 2 provides complementary evidence for the identified mineral phases.



Figure 1. Photographs of the rock specimens.

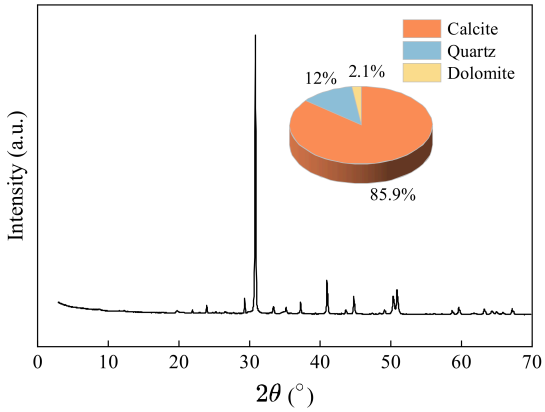


Figure 2. XRD results of specimens.

2.2. Experimental Equipment and Testing Procedure

Three acid systems commonly used in acid fracturing were tested: gelled acid, self-generating-acid (SGA)/gelled-acid composite system, and IVV acid. The Gelled acid consisted of 15 wt.% HCl, blended with 3.0 wt.% gelling agent. The viscosity was measured as 42 mPa·s at 140 °C. The SGA pre-fluid contained 12 wt.% ammonium salt and 10 wt.% organic ester, which slowly hydrolyses at high temperature to generate HCl in situ. The IVV acid included 15 wt.% HCl and 1.0 wt.% amphiphilic viscoelastic surfactant. The system exhibits variable viscosity triggered by acid–rock reaction. Its viscosity was 18 mPa·s at 140 °C. The two acid formulations were premixed before injection, and the resulting composite fluid was introduced as a single mixture. The tests were conducted with an LFDL-IV proppant fracture conductivity system (Figure 3) (manufactured by Haian Petroleum Scientific Research Instrument, Haian, China), which supports acid-etching experiments from room temperature to 140 °C and at flow pressures of 0–20 MPa. The slab conductivity cell and tubing are made of Hastelloy to withstand high-temperature, high-pressure corrosion. Before testing, the machined slabs were dried at 105 °C for 12 h in a constant-temperature oven and cooled to room temperature in a desiccator. The slabs were installed in the conductivity cell with an initial simulated fracture aperture of 1.5 mm. An applied closure pressure of 4 MPa was maintained during acid injection, and the outlet backpressure was held at 2 MPa. The cell and injection lines were heated to 140 °C and equilibrated for 2 h before acid injection. The outlet backpressure specifies the pressure at the downstream boundary; it does not imply a uniform fluid pressure throughout the fracture. The experimental conditions are listed in Table 1. Acid-displacement tests were conducted with gelled acid at 10, 20, and 40 mL/min using 1.0 L of acid; SGA + gelled acid at 20 mL/min using 1.0 L; and IVV acid at 20 mL/min using 0.5, 1.0, and 2.0 L. The acid experiment conditions are listed in Table 2. A constant outlet backpressure of 2 MPa was maintained to guarantee uniform contact between the acid and the slab surfaces. After acid injection, the heater was switched off, and the exhaust fan was used to cool the conductivity cell. The backpressure was then reduced to zero, and the tubing was flushed with distilled

water at 20 mL/min until pH paper indicated a neutral outlet. Finally, the cell was dismantled, and the specimens were removed, rinsed with clean water, and dried for subsequent testing. Each acid-etching condition was tested once using one pair of upper and lower rock slabs; no independent replicate acid-etching runs were performed.



Figure 3. LFDL-IV proppant fracture conductivity test system.

Table 1. Summary of experimental conditions for the rock-slab acid-etching tests.

Item	Value/Description
Specimen material	Siliceous limestone from a deep carbonate reservoir
Specimen size	178 mm × 38 mm × 25 mm
Pre-test drying	105 °C for 12 h; cooled in a desiccator
Initial simulated fracture aperture	1.5 mm
Closure pressure during acid injection	4 MPa
Outlet backpressure	2 MPa
Test temperature	140 °C; heated and equilibrated for 2 h before injection
Post-injection flush	Distilled water at 20 mL/min until neutral outlet pH

Table 2. Summary of experimental conditions for the acid conditions.

Acid System	Viscosity @140 °C (mPa·s)	Injection Rate (mL/min)	Acid Volume (L)
Gelled acid	42	10	1.0
Gelled acid	42	20	1.0
Gelled acid	42	40	1.0
SGA/gelled acid	11	20	1.0
IVV acid	18	20	0.5
IVV acid	18	20	1.0
IVV acid	18	20	2.0

2.3. Surface Morphology Characterization

A HeroScan L010 three-dimensional laser scanner was used to measure the slab surfaces before and after acid etching (manufactured by Haoyu 3D, Beijing, China) (Figure 4). The scanner has a data acquisition rate of 360,000 points/s and a nominal measurement accuracy of 0.1 mm. R_a and R_q are reported consistently to two decimal places for numerical comparison; this reporting precision does not imply a surface-height measurement accuracy of 0.01 mm. It operates on the time-of-flight (TOF) pulse-ranging principle: a laser beam rapidly scans the target, the reflected-light signal is recorded, and spatial coordinates are

calculated to generate a three-dimensional point-cloud model. The coordinates of laser footprint p are calculated as follows:

$$\begin{aligned} X_s &= S \times \cos\ (\theta) \times \cos\ (a) \\ Y_s &= S \times \cos\ (\theta) \times \sin\ (a) \\ Z_s &= S \times \sin\ (a) \end{aligned} \quad (1)$$

where S is the measured range, θ is the horizontal scan angle, and α is the vertical scan angle.



Figure 4. HeroScan L010 3D laser scanner.

The scanner was connected to a rotary stage, with the distance between them adjusted to approximately 450 mm. SLDSCAN V2.0 software was used to connect and calibrate the system. Each acid-etched slab was dried in a constant-temperature oven, and a thin layer of volatile developer was sprayed onto its surface to reduce reflections. The specimen was placed securely at the centre of the rotary stage and scanned through a full rotation. The resulting point-cloud data were exported, registered, denoised, and reconstructed with the supporting software to generate surface-elevation maps. These maps were used to quantify etching depth, surface roughness, and dissolution features such as wormholes, grooves, and sheet-like dissolution, thereby allowing the effects of the different acid systems on the siliceous limestone surfaces to be evaluated systematically.

2.4. Nanoindentation Tests

A Hysitron TI 980 TriboIndenter was used to measure the micromechanical properties of the siliceous limestone before and after acid etching (manufactured by Bruker Nano, Santa Barbara, CA, USA) (Figure 5). A Berkovich diamond indenter was adopted for all tests. The indentation array was arranged on the flat region of each fracture surface. The maximum indentation load was 50 mN. Loading and unloading were each performed over 10 s, corresponding to a constant load rate of 5 mN/s, with a holding period of 10 s at the maximum load. At least 15 valid indents were obtained on each tested specimen surface, with a minimum centre-to-centre spacing of 50 μm. To specifically characterize the mechanical weakening of calcite induced by acid etching, all nanoindentation points were deliberately positioned within individual calcite grains. Indents were placed sufficiently far from quartz grains and mineral grain boundaries to minimize the influence of quartz and interfacial effects on the measured mechanical response. Elastic modulus E and hardness H were calculated using the Oliver–Pharr method [14]. The unloading stiffness S is defined as:

$$S = \left.\frac{dP}{dh}\right|_{h=h_{max}} = \frac{2E_r\beta\sqrt{A}}{\sqrt{\Pi}} \quad (2)$$

where E_r is the reduced elastic modulus, which depends on the elastic moduli of the specimen and indenter; β is a constant related to indenter geometry; and A is the projected contact area of the indentation.



Figure 5. Nanoindentation test system.

The elastic modulus of the specimen is calculated as follows:

$$\frac{1}{E_r} = \frac{1-\mu^2}{E} + \frac{1-v_i^2}{E_i} \tag{3}$$

where E and μ are the elastic modulus and Poisson's ratio of the specimen, respectively, and E_i and ν_i are the known elastic modulus and Poisson's ratio of the indenter. In this test, $E_i = 1141$ GPa and $\nu_i = 0.07$.

The hardness of the specimen is calculated as:

$$H = \frac{p_{max}}{A} \tag{4}$$

The maximum contact area is the indenter-specimen contact area at the maximum load and is related to the contact depth h_c as follows:

$$A_m = f(h_c) = 3\sqrt{3h_C^2 \tan^2\theta} \approx 24.56h^2 \tag{5}$$

where θ is the equivalent half-cone angle of the indenter.

The indenter contact depth is calculated as follows:

$$h_c = h_{max} - r\frac{P_{max}}{S} \tag{6}$$

where γ is the geometric factor of the indenter.

The load-depth curve can be expressed as:

$$\begin{cases} P_{load} = Ch^2 \\ P_{unload} = k\left(h - h_f\right)^m \end{cases} \tag{7}$$

where C is the loading curvature, which depends on the specimen and indenter geometry, and k and m are fitting coefficients.

Differentiating at the maximum load according to Equation (2) gives the approximate contact stiffness S:

$$S = \frac{dP}{dh}\Big|_{h=h_{max}} = km\left(h_{max} - h_f\right)^{m-1} \tag{8}$$

Accordingly, the elastic modulus and hardness of the specimen can be calculated as follows:

$$\begin{cases} E = (1-\mu^2)\left(\frac{1}{E_r} - \frac{1-v_i^2}{E_i}\right)^{-1} \\ H = \frac{P_{max}}{A_m} \approx \frac{P_{max}}{24.56h_c^2} \end{cases} \tag{9}$$

Rock fracture toughness (Kc) was calculated using the indentation-energy method. Assuming that the dissipated energy consists of purely plastic deformation energy (U_{pp}) and fracture energy (Uc), Uc can be expressed as:

$$U_c = U_t - U_e - U_{pp} \tag{10}$$

U_{pp} and U_c can be calculated from:

$$\begin{cases} U_{pp} = [1 - \frac{1-3\left(\frac{h_f}{h_{max}}\right)^2+2\left(\frac{h_f}{h_{max}}\right)^3}{1-\left(\frac{h_f}{h_{max}}\right)^2}]U_t \\ U_t = \int_0^{h_{max}} P_c dh_c = \frac{P_{max}h_{max}}{3} \end{cases} \quad (11)$$

The critical energy-release rate can then be calculated as:

$$G_c = \frac{U_c}{A_{max}} \quad (12)$$

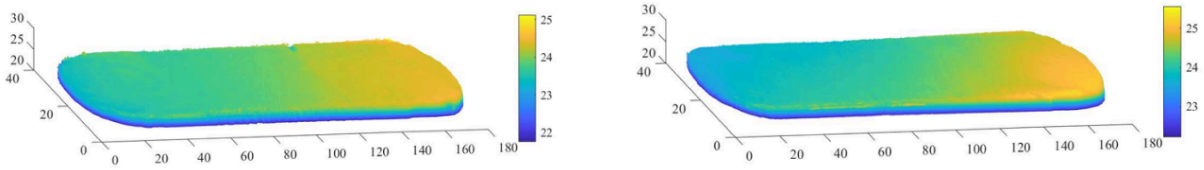
Finally, fracture toughness (K_c) is obtained in conjunction with Equation (5):

$$K_c = \sqrt{G_c E} \quad (13)$$

3. Analysis of Physical Properties

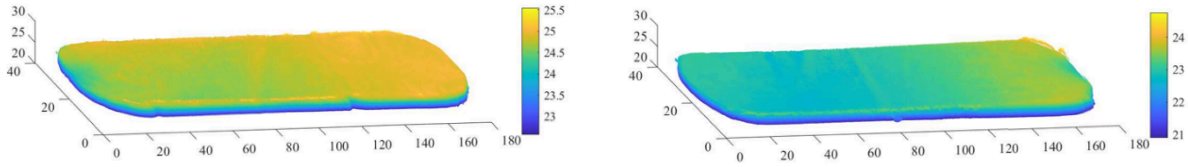
3.1. Evolution of Acid-Etched Surface Morphology

Figures 6–8 show surface-elevation maps of siliceous limestone slabs etched with different acid systems, injection rates, and acid volumes. Before acid etching, the slab surfaces were flat and showed no pronounced relief. After etching, dissolution features of varying intensity developed, with clear differences among acid types and operating conditions. In Figures 6–8, the horizontal axes indicate distances in millimetres, while the vertical axes and colour bars indicate surface elevation in millimetres.



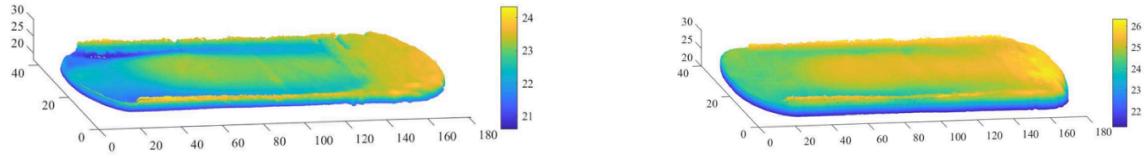
Upper slab Lower slab

(**a**) Gelled-acid injection rate: 10 mL/min



Upper slab Lower slab

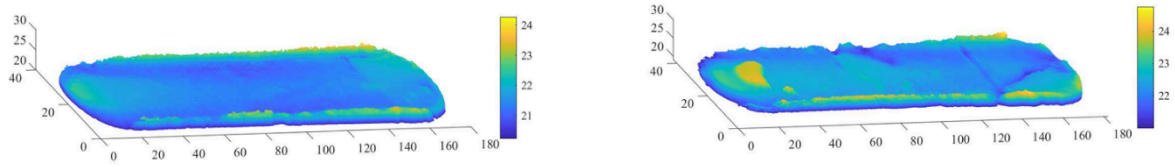
(**b**) Gelled-acid injection rate: 20 mL/min



Upper slab Lower slab

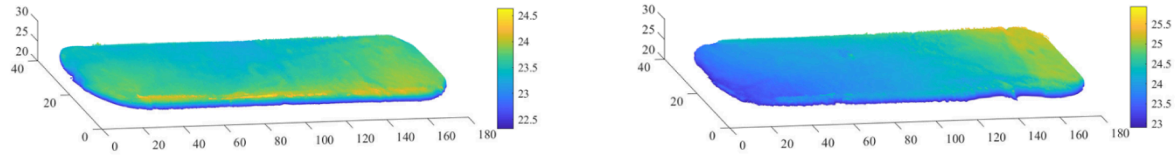
(**c**) Gelled-acid injection rate: 40 mL/min

Figure 6. Surface-elevation maps of the upper and lower slabs at different gelled-acid injection rates. (**a**) Gelled-acid injection rate: 10 mL/min; (**b**) Gelled-acid injection rate: 20 mL/min; (**c**) Gelled-acid injection rate: 40 mL/min.



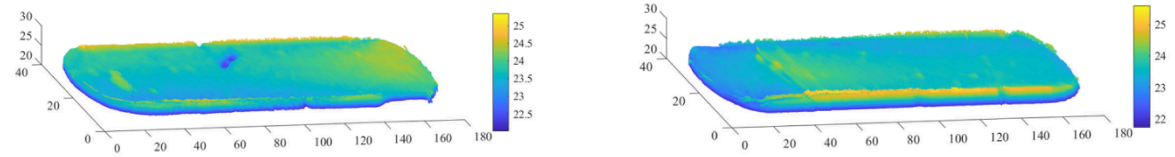
Upper slab Lower slab

Figure 7. Surface-elevation maps of the upper and lower slabs after treatment with self-generating acid + gelled acid.



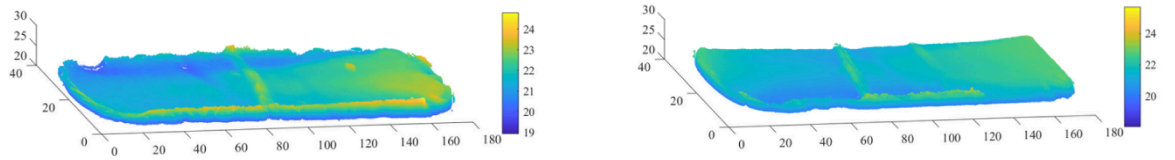
Upper slab Lower slab

(**a**) Acid volume: 0.5 L



Upper slab Lower slab

(**b**) Acid volume: 1.0 L



Upper slab Lower slab

(**c**) Acid volume: 2.0 L

Figure 8. Surface-elevation maps of the upper and lower slabs at different volumes of IVV acid. (**a**) Acid volume: 0.5 L; (**b**) Acid volume: 1.0 L; (**c**) Acid volume: 2.0 L.

With gelled acid (Figure 6a–c) and a constant acid volume of 1.0 L, dissolution became progressively more pronounced as the injection rate increased from 10 to 40 mL/min. At 10 mL/min, the surface remained relatively smooth, and the modification was limited. At 20 mL/min, both dissolution depth and affected area increased. At 40 mL/min, the surface relief became much stronger and typical wormhole-like dissolution channels developed.

Thus, at a constant acid volume, increasing the injection rate enhanced the dissolution of siliceous limestone by gelled acid.

With self-generating acid + gelled acid (Figure 7), an injection rate of 20 mL/min and an acid volume of 1.0 L produced pronounced surface dissolution in the siliceous limestone, with stronger morphological modification than gelled acid alone.

With IVV acid (Figure 8) at 20 mL/min, etching depth and overall dissolution increased steadily as the acid volume rose from 0.5 to 2.0 L. At 2.0 L, the surface showed the greatest relief and markedly deeper dissolution grooves. Acid volume therefore had a strong

influence on corrosion of the siliceous limestone, and increasing the volume effectively intensified dissolution by the IVV acid.

Comparison of the three acid systems indicates distinct dissolution responses under the tested conditions. IVV acid produced pronounced dissolution and relatively high tortuosity at the largest tested volume, whereas gelled acid at 40 mL/min produced the largest measured macroscopic roughness among the tested conditions. Because the acid formulations and operating conditions are not identical across all groups, direct ranking of dissolution intensity should be interpreted cautiously. The observed differences are plausibly related to acid viscosity, reaction rate, and mass-transfer behaviour, but these mechanisms were not independently measured in the present study.

Quantitative Analysis of Fracture-Surface Roughness

To quantify the effect of acid etching on the surface morphology of siliceous limestone fractures, the etched surfaces were evaluated across multiple scales using arithmetic mean roughness R_a, root-mean-square roughness R_q, fractal dimension D, and linear tortuosities ε_x and ε_y.

(a) Arithmetic mean and root-mean-square roughness:

Arithmetic mean roughness R_a and root-mean-square roughness R_q are conventional measures of the deviation of surface height from the mean. They describe the average amplitude and the intensity of surface-height fluctuations, respectively. Following Feng et al. [16], R_a and R_q were calculated from the three-dimensional laser-scanning elevation data using Equations (14) and (15):

$$R_a = \frac{1}{n}\sum_{i=1}^{n}\left|Z_i - \overline{Z}\right| \tag{14}$$

$$R_q = \sqrt{\frac{1}{n}\sum_{i=1}^{n}\left(Z_i - \overline{Z}\right)^2} \tag{15}$$

where Z_i is the height of point i, $\overline{Z}$ is the mean height, and n is the total number of points.

Table 3 lists the calculated R_a and R_q values for the upper and lower siliceous limestone slabs under the different acid systems. Before etching, both surfaces were flat, and R_a and R_q were close to zero. All values increased substantially after acid treatment, confirming that etching markedly altered the fracture-surface morphology.

Under gelled-acid treatment, R_a and R_q of both slabs varied non-monotonically as the injection rate increased from 10 to 40 mL/min. At 10 mL/min, R_a was 6.10 mm for the upper slab and 5.93 mm for the lower slab, while R_q was 7.07 and 6.88 mm, respectively. At 20 mL/min, R_a decreased to 5.37 mm for the upper slab and 2.51 mm for the lower slab, and R_q decreased to 6.25 and 2.98 mm. At 40 mL/min, R_a increased again to 6.38 and 6.08 mm, and R_q to 7.36 and 7.04 mm. These results indicate that at 20 mL/min the acid produced relatively uniform dissolution on the lower slab and a smoother surface, whereas at 40 mL/min it created heterogeneous, channel-like dissolution and stronger surface relief.

With IVV acid, roughness also changed non-monotonically as the acid volume increased from 0.5 to 2.0 L. At 0.5 L, R_a was 3.87 mm for the upper slab and 5.39 mm for the lower slab. At 1.0 L, it fell to minimum values of 2.94 and 0.65 mm, respectively. At 2.0 L, R_a rose again to 2.43 and 4.59 mm. This pattern indicates an acid volume of approximately 1.0 L, at which dissolution was relatively uniform, and surface flatness was greatest. Both smaller and larger volumes increased surface roughness.

For self-generating acid + gelled acid, R_a was 4.16 mm on the upper slab and 4.48 mm on the lower slab, while R_q was 4.85 and 5.23 mm, respectively. These values lay between those obtained with gelled acid and IVV acid.

Table 3. Surface roughness parameters of the upper and lower siliceous limestone slabs under different acid systems.

Acid System	Acid Injection Rate (mL/min)	Slab Position	Acid Volume (L)	R_a (mm)	R_q (mm)
Gelled acid	10	Upper slab	1	6.10	7.07
		Lower slab		5.93	6.88
	20	Upper slab	1	5.37	6.25
		Lower slab		2.51	2.98
	40	Upper slab	1	6.38	7.36
		Lower slab		6.08	7.04
SGA + gelled acid	20	Upper slab	1	4.16	4.85
		Lower slab		4.48	5.23
IVV acid	20	Upper slab	0.5	3.87	4.52
		Lower slab		5.39	6.28
		Upper slab	1	2.94	3.45
		Lower slab		0.65	1.02
		Upper slab	2	2.43	3.03
		Lower slab		4.59	5.36

Across the tested conditions, the highest macroscopic roughness occurred with gelled acid at 40 mL/min, whereas the lowest lower-slab R_a occurred with 1.0 L of IVV acid. These observations demonstrate that acid formulation and operating conditions strongly influence surface morphology, but they do not by themselves establish an optimal condition for fracture conductivity.

(b) Surface fractal dimension:

Fractal dimension D describes surface complexity and self-similarity and is therefore an effective roughness metric. Following Chen [17], D was calculated using a cubic box-counting method. The projected XOY plane was divided into square grids of side length δ, and the total number of cubes N_δ required to cover the surface was counted. The box sizes used in the analysis were δ= 0.1, 0.2, 0.4, 0.8, 1.6 and 3.2 mm. For a fractal surface, N_δ scales with δ-D. Linear regression in log–log coordinates gives D from the slope, while the coefficient of determination R^2 indicates the strength of the fractal scaling.

Table 4 presents the fractal dimensions of the upper- and lower-slab surfaces under the different acid systems. The coefficient of determination R^2 exceeded 0.998 for every specimen, indicating well-defined fractal behaviour of the acid-etched surfaces. The number of cubic boxes N_δ obtained at each box size is listed in Table 5.

Table 4. Surface fractal dimensions of siliceous limestone under different acid systems.

Acid System	Acid Injection Rate (mL/min)	Slab Position	Acid Volume (L)	D	R^2
Gelled acid	10	Upper slab	1	2.001	0.99996
		Lower slab		2.005	0.99995
	20	Upper slab	1	2.010	0.99996
		Lower slab		2.051	0.99997
	40	Upper slab	1	2.083	0.99998
		Lower slab		2.072	0.99987

Table 4. *Cont.*

Acid System	Acid Injection Rate (mL/min)	Slab Position	Acid Volume (L)	D	R^2
SGA + gelled acid	20	Upper slab	1	2.041	0.99995
		Lower slab		2.026	0.99991
IVV acid	20	Upper slab	0.5	2.019	0.99996
		Lower slab		1.993	0.99996
		Upper slab	1	2.089	0.99993
		Lower slab		2.117	0.99985
		Upper slab	2	2.150	0.99970
		Lower slab		2.094	0.99986

Table 5. Number of cubic boxes at different box sizes for each acid-etched fracture surface.

Specimen	$N\delta$ at Box Size δ (mm)					
	0.1	0.2	0.4	0.8	1.6	3.2
Gelled acid, 10 mL/min, 1 L, upper slab	722,623	187,215	46,613	11,636	2910	704
Gelled acid, 10 mL/min, 1 L, lower slab	728,544	189,594	46,985	11,777	2889	704
Gelled acid, 20 mL/min, 1 L, upper slab	750,459	191,432	47,036	11,639	2959	704
Gelled acid, 20 mL/min, 1 L, lower slab	882,753	218,222	51,333	12,262	3068	724
Gelled acid, 40 mL/min, 1 L, upper slab	968,244	233,369	53,624	12,636	3038	715
Gelled acid, 40 mL/min, 1 L, lower slab	1,055,505	253,973	58,183	13,777	3215	832
SGA + gelled acid, 20 mL/min, 1 L, upper slab	821,975	211,471	50,327	12,165	2937	710
SGA + gelled acid, 20 mL/min, 1 L, lower slab	765,514	202,548	48,384	11,658	2864	706
IVV acid, 20 mL/min, 0.5 L, upper slab	749,852	191,331	45,891	11,203	2764	705
IVV acid, 20 mL/min, 0.5 L, lower slab	684,850	177,979	43,758	10,791	2718	702
IVV acid, 20 mL/min, 1 L, upper slab	964,130	223,246	51,023	11,926	2868	696
IVV acid, 20 mL/min, 1 L, lower slab	1,073,089	262,721	57,204	12,937	2982	735
IVV acid, 20 mL/min, 2 L, upper slab	1,314,899	317,147	66,271	14,332	3298	817
IVV acid, 20 mL/min, 2 L, lower slab	1,155,764	293,479	65,171	14,821	3519	856

Before acid etching, the surface fractal dimension was close to 2.0, consistent with a relatively flat surface. After etching, D increased markedly for every specimen, ranging from 1.993 to 2.150 and indicating rough-surface characteristics.

With gelled acid, D was 2.001 for the upper slab and 2.005 for the lower slab at 10 mL/min. It increased to 2.010 and 2.051 at 20 mL/min and to 2.083 and 2.072 at 40 mL/min. This pattern differs from the trends in R_a and R_q, which were non-monotonic.

With IVV acid, D was 2.019 for the upper slab and 1.993 for the lower slab at an acid volume of 0.5 L. At 1.0 L, it increased to 2.089 for the upper slab and 2.117 for the lower slab. At 2.0 L, the values were 2.150 and 2.094, respectively. Notably, at 1.0 L, R_a was lowest even though D was high. This combination suggests that numerous fine asperities and micropits formed: the overall height variation remained small, but the microscale structure was complex, resulting in a high fractal dimension.

For self-generating acid + gelled acid, D was 2.041 on the upper slab and 2.026 on the lower slab, again lying between the values associated with gelled acid and IVV acid.

(c) Tortuosity:

Linear tortuosity is an important measure of surface curvature in a specified direction and can be used to quantify the sinuosity of the acid-flow path. Following Dai and Hou [18], ε_x and ε_y were defined as the linear tortuosities in the acid-flow direction (X) and the transverse direction (Y), respectively:

$$\varepsilon = \frac{L}{L_0} \tag{16}$$

where L is the actual length of the profile in the specified direction, and L_0 is its projected straight-line length. A value of ε close to one indicates a nearly straight surface profile; larger values indicate greater curvature.

Table 6 presents the linear tortuosities of the upper- and lower-slab surfaces under the different acid systems. Before etching, ε_x and ε_y were both close to 1.00, consistent with a flat surface. After etching, tortuosity increased in every specimen, and ε_y was consistently greater than ε_x. The surface was therefore more curved transverse to the flow than along it, in agreement with the grooves observed in Figures 6–8: the grooves developed in the flow direction, while wave-like relief formed across the flow.

Table 6. Surface tortuosity parameters of siliceous limestone under different acid systems.

Acid System	Acid Injection Rate (mL/min)	Slab Position	Acid Volume (L)	ε_x	ε_y
Gelled acid	10	Upper slab	1	1.026	1.033
		Lower slab		1.025	1.030
	20	Upper slab	1	1.033	1.039
		Lower slab		1.056	1.067
	40	Upper slab	1	1.108	1.140
		Lower slab		1.102	1.124
SGA + gelled acid	20	Upper slab	1	1.081	1.107
		Lower slab		1.090	1.112
IVV acid	20	Upper slab	0.5	1.040	1.045
		Lower slab		1.038	1.046
		Upper slab	1	1.105	1.122
		Lower slab		1.162	1.183
		Upper slab	2	1.275	1.332
		Lower slab		1.183	1.243

With gelled acid, increasing the injection rate from 10 to 40 mL/min raised ε_x from 1.025 to 1.026 to 1.102–1.108 and ε_y from 1.030 to 1.033 to 1.124–1.140. Tortuosity increased continuously, unlike the non-monotonic trend in R_a. Thus, although surface roughness declined at 20 mL/min, the overall flow path continued to become more sinuous, reflecting a gradual shift from uniform to channel-like dissolution.

With IVV acid, increasing the acid volume from 0.5 to 2.0 L raised ε_x from 1.038 to 1.040 to 1.183–1.275 and ε_y from 1.045 to 1.046 to 1.243–1.332. At 2.0 L, the upper slab reached $\varepsilon_x = 1.275$ and $\varepsilon_y = 1.332$, the highest values of all specimens, indicating the most complex flow path.

For self-generating acid + gelled acid, ε_x ranged from 1.081 to 1.090 and ε_y from 1.107 to 1.112, intermediate between the other two acid systems.

3.2. Effect of Acid Etching on Micromechanical Properties

3.2.1. Load–Displacement Curves

Figure 9 presents the nanoindentation load–displacement curves of untreated siliceous limestone used as the reference for the gelled-acid tests. The untreated specimens showed relatively steep loading curves and indentation depths of approximately 1500 nm. These curves describe the local indentation response of the tested calcite regions. The decrease in

load after the maximum corresponds to the unloading stage and should not, by itself, be interpreted as evidence of brittle failure.

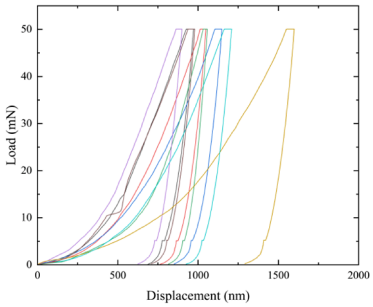


Figure 9. Load–displacement curve of siliceous limestone before gelled-acid etching. (different colored lines denote different nanoindentation test points).

Acid etching changed the measured load–displacement response. After treatment with gelled acid at 10 mL/min (Figure 10a), the indentation depth exceeded 4000 nm, and the loading slope decreased relative to the untreated reference. The curves obtained at the other injection rates also showed greater penetration than the untreated reference. Together with the reductions in elastic modulus and hardness reported in Section 3.2.2, these observations indicate local softening and increased deformability under indentation.

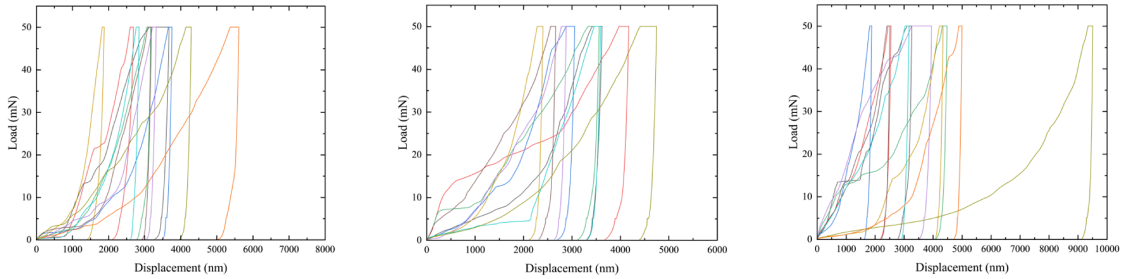


Figure 10. Load–displacement curves of siliceous limestone after gelled-acid etching. (**a**) Gelled-acid injection rate: 10 mL/min; (**b**) Gelled-acid injection rate: 20 mL/min; (**c**) Gelled-acid injection rate: 40 mL/min. Different colored lines represent the curves obtained from different nanoindentation test points. (different colored lines denote different nanoindentation test points).

Figures 11 and 12 compare the untreated reference and the specimens treated with different volumes of IVV acid. The post-etching curves showed greater penetration than the untreated reference, indicating an altered local indentation response. Differences among the tested volumes should be considered together with the calculated mechanical parameters rather than interpreted from curve shape alone as a monotonic increase in damage.

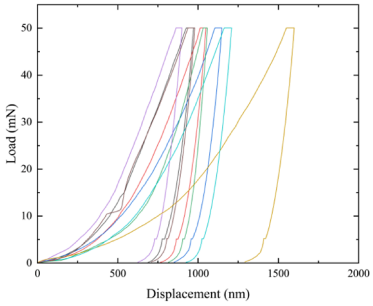


Figure 11. Load–displacement curve of siliceous limestone before treatment with IVV acid. (different colored lines denote different nanoindentation test points).

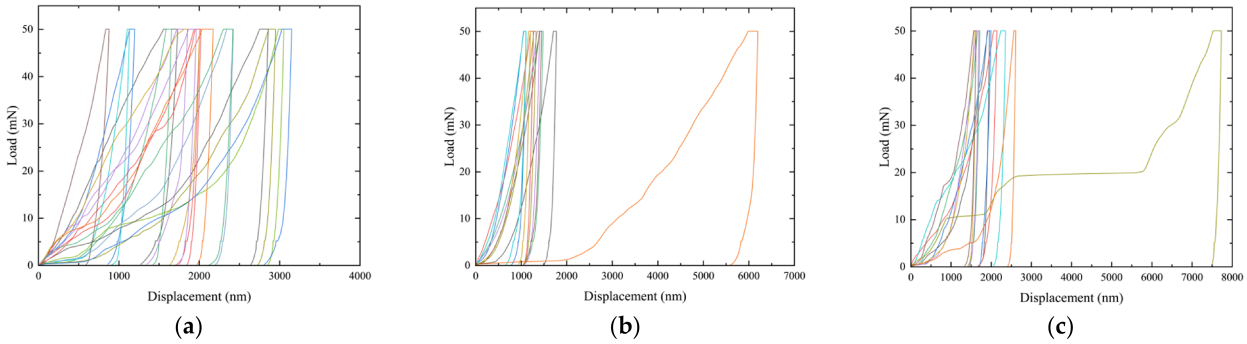


Figure 12. Load–displacement curves at different volumes of IVV acid. (**a**) Acid volume: 0.5 L; (**b**) Acid volume: 1.0 L; (**c**) Acid volume: 2.0 L. (different colored lines denote different nanoindentation test points).

The premixed SGA/gelled-acid composite system also produced greater indentation depths than the untreated reference (Figure 13), reaching approximately 3000–4000 nm. This response is consistent with the reductions in local mechanical properties reported in Section 3.2.2. However, the loading and unloading curves alone do not establish a change in the macroscopic failure mode.

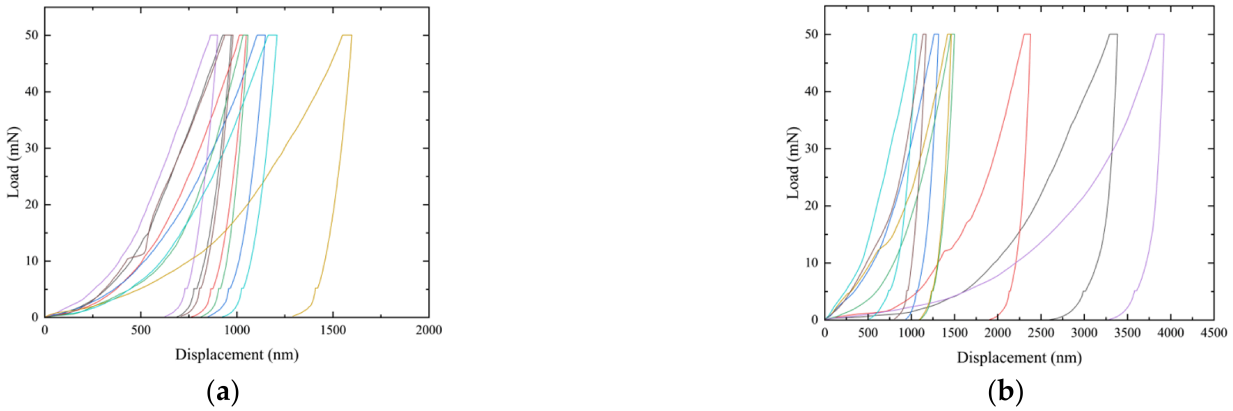


Figure 13. Load–displacement curves of siliceous limestone before and after treatment with self-generating acid + gelled acid. (**a**) Before acid etching; (**b**) After acid etching. (different colored lines denote different nanoindentation test points).

The measured changes provide evidence of local mechanical weakening following acid treatment. Preferential calcite dissolution and associated changes in porosity, microcracking, and grain bonding offer possible explanations, consistent with the broader acid-induced weakening of carbonate rocks discussed in previous studies [11,12]. However, these microstructural processes were not directly characterized in the present experiments. In particular, neither the presence nor the thickness of a distinct softened near-surface layer was established. These mechanisms are therefore proposed as interpretations of the measured response rather than directly observed features.

3.2.2. Quantitative Analysis of Mechanical Parameters

Table 7 summarizes the elastic modulus, hardness, and fracture toughness of siliceous limestone before and after gelled-acid etching. Before etching, the elastic modulus was 72.39 GPa, the hardness was 1.85 GPa, and the fracture toughness was 5.76 MPa·m½.

Table 7. Mechanical parameters of siliceous limestone at different gelled-acid injection rates.

Rock Type	Acid Injection Rate (mL/min)	Elastic Modulus (GPa)	Hardness (GPa)	Fracture Toughness (MPa√m)
Siliceous limestone	Before acid etching	72.39	1.85	5.76
	10	24.27	0.25	1.36
	20	30.06	0.21	1.36
	40	27.69	0.24	1.43

After etching at injection rates of 10, 20, and 40 mL/min, the elastic modulus decreased to 24.27, 30.06, and 27.69 GPa, respectively, representing reductions of 58.2–66.5%. Hardness decreased to 0.25, 0.21, and 0.24 GPa, reductions of 86.5–88.6%, while fracture toughness decreased to 1.36, 1.36, and 1.43 MPa·m½, reductions of 75.2–76.4%.

As shown in Table 8, self-generating acid + gelled acid caused a clear deterioration in the mechanical properties of the siliceous limestone. Elastic modulus fell from 72.39 to 36.34 GPa, a reduction of 49.8%; hardness fell from 1.85 to 0.94 GPa, a reduction of 49.2%; and fracture toughness fell from 5.76 to 3.58 MPa·m½, a reduction of 37.8%. The mechanical damage was less severe than that caused by gelled acid alone but remained substantial.

Table 8. Mechanical parameters of siliceous limestone treated with self-generating acid + gelled acid.

Rock Type	Treatment Condition	Elastic Modulus (GPa)	Hardness (GPa)	Fracture Toughness (MPa√m)
Siliceous limestone	Before acid etching	72.39	1.85	5.76
	After acid etching	36.34	0.94	3.58

As shown in Table 9, after treatment with 0.5, 1.0, and 2.0 L of IVV acid, the elastic modulus decreased to 54.55, 63.86, and 50.88 GPa, respectively, corresponding to reductions of 11.8–29.7%. Hardness decreased to 1.13, 1.21, and 0.60 GPa, reductions of 34.6–67.6%, while fracture toughness decreased to 4.32, 4.68, and 2.61 MPa·m½, reductions of 18.8–54.7%.

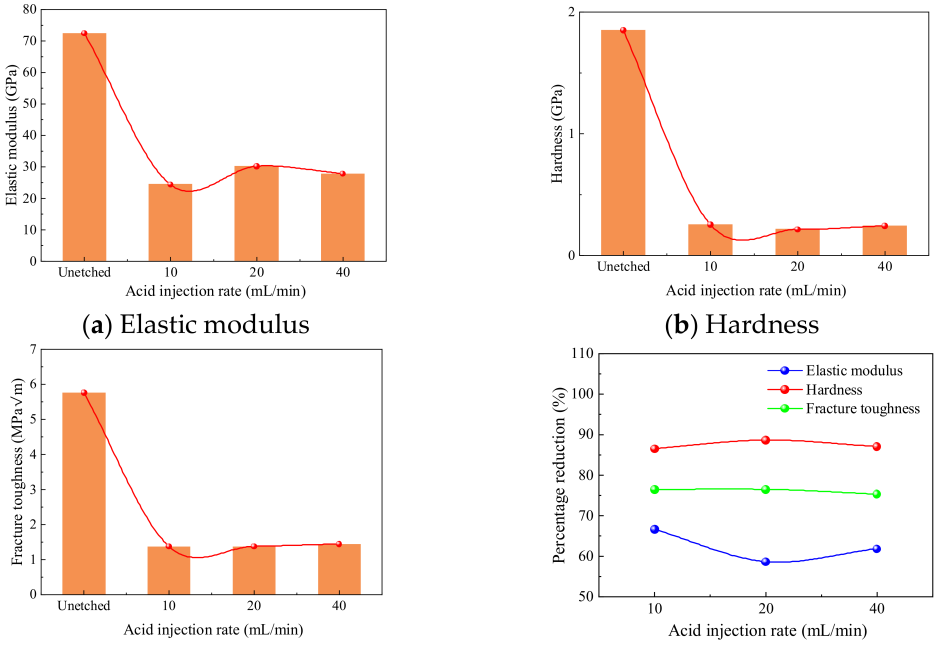
Table 9. Mechanical parameters of siliceous limestone at different volumes of IVV acid.

Rock Type	Acid Volume (L)	Elastic Modulus (GPa)	Hardness (GPa)	Fracture Toughness (MPam½)
Siliceous limestone	Before acid etching	72.39	1.85	5.76
	0.5	54.55	1.13	4.32
	1.0	63.86	1.21	4.68
	2.0	50.88	0.60	2.61

Figures 14 and 15 compare the percentage reductions in the mechanical parameters under the different acid-etching conditions. Gelled acid caused the most severe degradation, followed by IVV acid. Of the three parameters, hardness consistently showed the largest reduction. In the present tests, localized resistance to indentation was therefore more sensitive to acid attack than the elastic response.

The sharp decline in hardness is directly related to the formation of the surface softening layer. Dissolution of calcite loosens the near-surface structure, promotes micropore development, weakens interparticle bonding, and markedly reduces resistance to indentation. The decrease in elastic modulus reflects a loss of overall rock stiffness: calcite dissolution

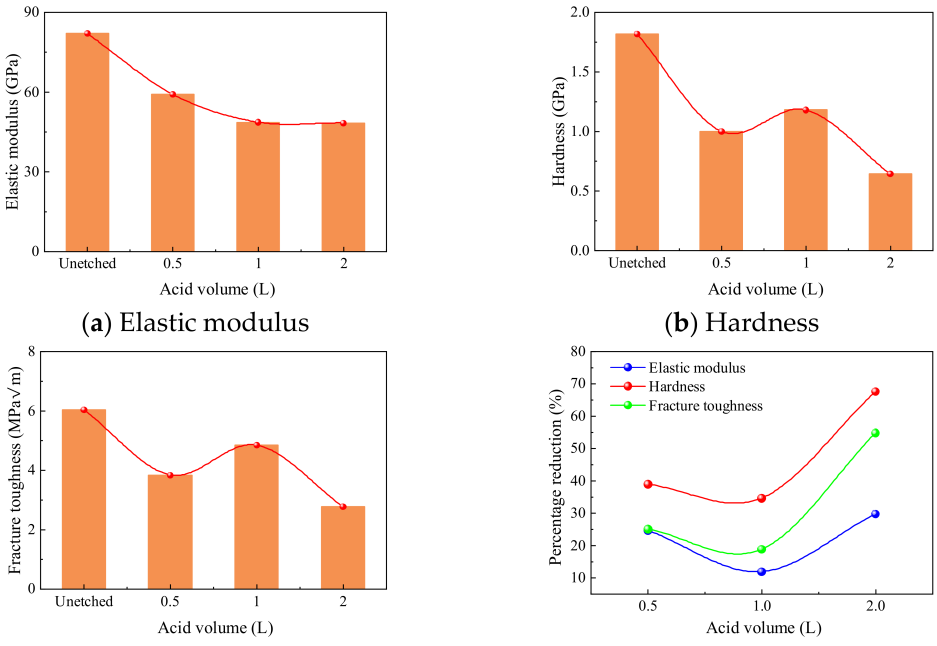
disrupts the continuity of the stress-transfer network, allowing the rock to deform more readily under load. The decrease in fracture toughness indicates reduced resistance to crack propagation, with acid-induced microcracks acting as stress concentrators. Together, these changes demonstrate the comprehensive mechanical damage caused by acid etching.



(**a**) Elastic modulus (**b**) Hardness

(**c**) Fracture toughness (**d**) Percentage reduction

Figure 14. Reductions in mechanical parameters at different gelled-acid injection rates. (The red line connects the average values at different acid injection rates).



(**a**) Elastic modulus (**b**) Hardness

(**c**) Fracture toughness (**d**) Percentage reduction

Figure 15. Reductions in mechanical parameters at different volumes of IVV acid. (The red line connects the average values at different acid injection volume).

The mechanical weakening observed here is qualitatively consistent with the deterioration of carbonate-rock mechanical properties under acidified conditions reported by Zhang et al. [12]. However, the measurement scale must be considered when comparing

results. Zhou et al. [13] used scratch tests to investigate acid-fracture-surface strength and highlighted the roles of acid reactivity and mineral composition. Their surface-focused approach complements the present nanoindentation measurements, which characterize selected calcite regions rather than the collective response of the heterogeneous fracture surface. Abdallah et al. [15] combined nanoindentation with SEM–EDS to relate local elastic properties to carbonate-rock microstructure and showed that translating local measurements into macroscopic elastic properties requires additional consideration of microstructural features. Accordingly, the modulus and hardness values reported here should be interpreted as local indentation properties rather than bulk-rock properties.

The present study extends this surface-focused characterization by examining acid etching at 140 °C and considering the measured surface geometry alongside calcite-grain mechanical properties. In particular, the comparatively low roughness obtained with gelled acid at 20 mL/min coexisted with substantial reductions in local modulus and hardness. This observation supports the need to distinguish geometric modification from mechanical preservation. Direct numerical comparison with previous studies remains limited by differences in lithology, acid composition, exposure conditions, measurement scale, and testing method; the agreement discussed here therefore concerns the general weakening trend rather than equivalence between the measured property values.

3.3. Comprehensive Damage Index and Morphology–Mechanics Relationship

Acid treatment modifies siliceous limestone fracture surfaces in two ways. First, dissolution creates a heterogeneous surface geometry. Second, acid-induced damage to the near-surface microstructure reduces elastic modulus, hardness, and fracture toughness. These effects are not independent; they are two outcomes of the same chemical process. Examining morphological and mechanical parameters together therefore provides a more complete characterization of acid-induced fracture-surface modification than either group of parameters alone.

3.3.1. Morphology–Mechanics Relationship

Comparison of Tables 3 and 7 reveals a clear inverse relationship between R_a and E. R_a was highest and the elastic-modulus reduction greatest with gelled acid at 40 mL/min, whereas both R_a and the elastic-modulus reduction were lowest with 1.0 L of IVV acid. Under the latter condition, however, D remained high and hardness decreased by 34.6%. Thus, despite modest overall relief, the complex microstructure and development of micropores and microcracks caused a substantial local loss of hardness. A similar inverse trend is evident between ε_y in Table 6 and K_c in Table 7: greater surface-path tortuosity is associated with more extensive microcracking and weaker resistance to crack propagation.

The modification mechanism can therefore be summarized as follows. Active acid selectively dissolves calcite, simultaneously creating heterogeneous dissolution morphology and loosening the near-surface structure through micropore development. Because these are two manifestations of the same chemical process, their spatial distributions are consistent: morphological parameters are greatest in the dissolution grooves, where the mechanical parameters also show the largest reductions.

3.3.2. Comprehensive Damage Index

A comprehensive damage index, D_T, was formulated by combining the relative changes in elastic modulus E, hardness H, and fracture toughness K with the etching-depth influence factor. The three mechanical parameters are combined through a parallel coupling factor, which is subsequently coupled with the etching-depth influence factor to characterize the

joint changes in surface mechanical properties and geometry. Damage to each mechanical parameter is defined as:

$$\begin{cases} D_E = 1 - \frac{E}{E_0} \\ D_H = 1 - \frac{H}{H_0} \\ D_K = 1 - \frac{K}{K_0} \end{cases} \tag{17}$$

The etching-depth influence factor is defined as:

$$D_d = 1 - \frac{d}{d_0} \tag{18}$$

The parallel coupling factor for the mechanical parameters is:

$$D_M = \prod_{i=1}^{3} (1 - D_i)^{\zeta_i},\ D_1 = D_E,\ D_2 = D_H,\ D_3 = D_K \tag{19}$$

In this formulation, the parallel coupling factor for the mechanical parameters is expressed as a weighted product of the normalized retention ratios of elastic modulus, hardness, and fracture toughness. It can therefore be interpreted as a weighted mechanical-property retention factor within the proposed coupling model. The weighting coefficients were determined through multiple regression using the measured local mechanical parameters and corresponding depth data. The index follows a retention-based convention: one represents the undamaged state, whereas zero represents complete deterioration.

The comprehensive damage factor is defined as:

$$D_T = 1 - (1 - D_M)(1 - D_d) \tag{20}$$

The comprehensive damage factor combines the parallel coupling factor of the mechanical parameters with the etching-depth influence factor. In the selected coupling form, the reduction in combined mechanical-property retention is scaled by the normalized etching depth. This phenomenological formulation accounts for the joint influence of mechanical degradation and geometrical modification, while preserving the undamaged reference value when all three mechanical properties are fully retained.

The calculated comprehensive damage index varied with the acid-treatment conditions. At a gelled-acid injection rate of 40 mL/min, D_T reached 0.72–0.85; with 2.0 L of IVV acid, it reached 0.55–0.68.

The comprehensive damage index reflected the combined influence of surface mechanical properties and etching depth. Within the proposed coupling model, lower D_T values indicated greater combined deterioration, whereas higher values indicated greater retention. The index therefore provided an integrated characterization of the mechanical and geometrical changes induced by acid etching.

3.3.3. Morphology–Mechanics Characteristics of the Acid Systems

(a) Gelled acid: sheet-like uniform dissolution with local grooves

At a gelled-acid injection rate of 20 mL/min, R_a on the lower slab was only 2.51 mm, and D was 2.051, yet elastic modulus and hardness decreased by 58.5% and 88.6%, respectively. The surface was comparatively smooth despite severe mechanical damage. This indicates sheet-like, relatively uniform dissolution: no deep grooves formed, but the microstructure deteriorated markedly and local mechanical weakening was measured. At 40 mL/min, deep grooves formed, R_a increased to 6.08 mm, elastic modulus decreased by 61.7%, and hardness decreased by 87.0%; both morphological and mechanical damage approached their maximum levels.

(b) IVV acid: fine, uniform dissolution

With 1.0 L of IVV acid, R_a on the lower slab was only 0.65 mm, but D reached 2.117 and hardness decreased by 34.6%. The surface was macroscopically smooth but microscopically complex. At this volume, the acid formed numerous fine, uniformly distributed dissolution pits, producing little overall relief but substantial microscale complexity. At 2.0 L, R_a increased to 4.59 mm, D decreased to 2.094, and hardness decreased by 67.6%, indicating that excessive dissolution created deep grooves and further degraded the microstructure.

(c) Self-generating acid + gelled acid: intermediate modification

With self-generating acid + gelled acid, R_a ranged from 4.16 to 4.48 mm, D from 2.026 to 2.041, while elastic modulus and hardness decreased by 49.8% and 49.2%, respectively. All parameters lay between those for gelled acid and IVV acid, indicating an intermediate degree of modification.

3.3.4. Grey Correlation Analysis

Grey correlation analysis was used to evaluate the sequence similarity between the morphological parameters R_a, D, ε_x, and ε_y and the mechanical parameters E, H, and K_c within the present dataset. Following Deng [19], the mechanical parameters were taken as the reference sequences and the morphological parameters as the comparison sequences.

Let the first sequence represent a mechanical parameter and the second a morphological parameter. The relational coefficient is given by Equation (21):

$$\begin{cases} X_0 = \{X_0(k), k = 1, 2, \ldots, m\} \\ X_i = \{X_i(k), k = 1, 2, \ldots, m; i = 1, 2, \ldots, n\} \zeta_i(k) \\ \zeta_i(k) = \frac{minimink|X_i(k) - X_0(k)| + \rho maximaxk|X_i(k) - X_0(k)|}{|X_i(k) - X_0(k)| + \rho maximaxk|X_i(k) - X_0(k)|} \end{cases} \quad (21)$$

where ρ is the distinguishing coefficient and was set to 0.5 in this study.

The correlation grade r_i is calculated as:

$$r_i = \frac{1}{m} \sum_{k=1}^{m} \zeta_i(k) \quad (22)$$

A higher grey relational grade indicates greater sequence similarity under the adopted preprocessing and calculation procedure.

Table 10 summarizes the grey relational grades obtained for the present dataset. Fractal dimension D had the highest mean relational grade across the three mechanical parameters 0.84, and the D–H pair had the highest individual grade 0.88. These results identify D as the morphological descriptor with the greatest sequence similarity to the mechanical parameters under the adopted analysis procedure. They do not establish that D controls mechanical weakening or that increasing D necessarily causes hardness to decrease. Likewise, the lower grades obtained for R_a cannot be interpreted as evidence of a limited causal influence of macroscopic roughness on fracture resistance. The rankings are descriptive and specific to the tested specimens, operating conditions, and data-processing choices. Their general applicability requires assessment using additional independent datasets.

Table 10. Grey correlation grades between morphological and mechanical parameters.

Parameter	$r(E)$	$r(H)$	$r(K_c)$	Mean r
R_a	0.71	0.68	0.71	0.70
D	0.82	0.88	0.83	0.84
ε_x	0.69	0.65	0.67	0.67
ε_y	0.82	0.79	0.78	0.80

3.3.5. Implications and Limitations of the Comprehensive Damage Index

The comprehensive damage index D_T combines etching depth with losses in the measured local mechanical properties. It provides a descriptive means of comparing geometric modification and mechanical degradation under the tested conditions. The results highlight that comparatively low macroscopic roughness does not necessarily indicate preservation of local mechanical properties. Surface morphology and micromechanical measurements should therefore be considered together when characterizing acid-etched siliceous limestone.

The index has not been calibrated against fracture conductivity and should not be interpreted as a predictor of conductivity or its long-term retention. Although a closure pressure was applied during acid etching, conductivity evolution under closure was not measured. In addition, nanoindentation within selected calcite grains does not directly quantify the collective load-bearing response of the heterogeneous fracture surface. Consequently, the present results do not establish which acid system provides the highest initial conductivity or the greatest long-term conductivity retention. Conductivity tests under a range of closure stresses, together with sustained-loading measurements, are needed to evaluate whether the observed morphological and local mechanical changes translate into differences in fracture-scale hydraulic performance.

4. Conclusions

High-temperature, high-pressure rock-slab acid-etching tests, three-dimensional laser scanning, and nanoindentation were used to investigate how acid etching affects the surface mechanical properties of siliceous limestone fractures. The main conclusions are as follows:

(1) Acid etching markedly altered fracture-surface morphology. At a gelled-acid injection rate of 20 mL/min, R_a on the lower slab decreased to 2.51 mm; with 1.0 L of IVV acid, it decreased to 0.65 mm, producing comparatively smooth surfaces. At 40 mL/min with gelled acid, R_a reached 6.38 mm, while 2.0 L of IVV acid produced $\varepsilon_y = 1.332$ and channel-like heterogeneous dissolution. For every specimen, ε_y exceeded ε_x, indicating greater curvature transverse to the acid-flow direction.

(2) Acid etching substantially degraded the micromechanical properties of the fracture surfaces. Gelled acid reduced elastic modulus by as much as 66.5%, hardness by 88.6%, and fracture toughness by 76.4%. IVV acid produced maximum reductions of 29.7%, 67.6%, and 54.7%, respectively. Hardness showed the largest decline, indicating pronounced local mechanical weakening as the clearest expression of mechanical degradation. The increased indentation depth and reduced loading slope after acid treatment indicate local softening and increased deformability, consistent with the measured losses in elastic modulus and hardness.

(3) A comprehensive damage index, D_T, coupling etching depth with mechanical parameters was established to quantify the combined modification of fracture-surface geometry and mechanical properties. D_T ranged from 0.72 to 0.85 for gelled acid at 40 mL/min and from 0.55 to 0.68 for IVV acid at an injected volume of 2.0 L, reflecting the combined influence of mechanical-property changes and etching depth. Within the present dataset, fractal dimension D had the highest mean grey relational grade among the examined mechanical parameters, and the highest individual grade occurred between D and hardness. These rankings describe associations under the adopted analysis procedure.

(4) The acid systems affected siliceous limestone in distinctly different ways. IVV acid produced the strongest dissolution and the greatest surface relief, whereas gelled acid caused the most severe mechanical damage, with larger reductions in elastic modulus and hardness. These results support joint characterization of surface morphology and local

mechanical properties when evaluating acid-induced fracture-surface modification. Their implications for fracture conductivity under closure require direct experimental validation.

Author Contributions: Conceptualization, Z.L. and Y.C.; methodology, Z.L. and Y.C.; software, H.P. and X.L.; validation, J.Y., Y.L. and R.Y.; formal analysis, Y.J.; investigation, Z.L., J.Y., H.P., Y.L., X.L., R.Y. and Y.J.; resources, Y.C.; data curation, H.P. and X.L.; writing—original draft preparation, Z.L.; writing—review and editing, Y.J. and Y.C.; visualization, H.P. and X.L.; supervision, Y.C.; project administration, Y.C.; funding acquisition, Y.C. All authors have read and agreed to the published version of the manuscript.

Funding: This research was funded by the Jiangsu Province Young Scientific and Technological Talents Support Project of 2024 (KJ20250038).

Data Availability Statement: The original contributions presented in this study are included in the article. Further inquiries can be directed to the corresponding author.

Conflicts of Interest: Authors Ze Li, Jian Yang, Huan Peng, Yuntao Liu, Xu Liu, Ruoyu Yang and Yucheng Jia are employed by PetroChina Southwest Oil & Gas Field Company. The remaining authors declare that the research was conducted in the absence of any commercial or financial relationships that could be construed as potential conflicts of interest.

References

1. Aljawad, M.S.; Aljulaih, H.; Mahmoud, M.; Desouky, M. Integration of field, laboratory, and modeling aspects of acid fracturing: A comprehensive review. *J. Pet. Sci. Eng.* **2019**, *181*, 106158. [CrossRef]
2. Gou, B.; Liu, Z.; Zhou, J.; Xu, K.; Xiao, B.; Pu, K.; Guo, J. Experimental and modeling study on the acid-etching and conductivity of hydraulic fractures in carbonate rocks: A critical review. *Geoenergy Sci. Eng.* **2025**, *245*, 213517. [CrossRef]
3. Li, N.; Feng, Y.; Liu, P.; Luo, Z.; Zhao, L. Study of acid–rock reaction kinetics under high temperature and pressure conditions based on the rotating disk instrument. *Arab. J. Sci. Eng.* **2015**, *40*, 135–142. [CrossRef]
4. Zhang, R.; Hou, B.; Zhou, B.; Liu, Y.; Xiao, Y.; Zhang, K. Effect of acid fracturing on carbonate formation in southwest China based on experimental investigations. *J. Nat. Gas Sci. Eng.* **2020**, *73*, 103057. [CrossRef]
5. Asadollahpour, E.; Baghbanan, A.; Hashemolhosseini, H.; Mohtarami, E. The etching and hydraulic conductivity of acidized rough fractures. *J. Pet. Sci. Eng.* **2018**, *166*, 704–717. [CrossRef]
6. Li, Q.; Chen, W.; Lu, Y.; Xiao, Q. Etched surface morphology analysis experiments under different reaction rates. *J. Pet. Sci. Eng.* **2019**, *172*, 517–526. [CrossRef]
7. Lu, C.; Bai, X.; Luo, Y.; Guo, J. New study of etching patterns of acid-fracture surfaces and relevant conductivity. *J. Pet. Sci. Eng.* **2017**, *159*, 135–147. [CrossRef]
8. Rodríguez, X.; Barbosa, A.; Cardona, A.; Guimarães, L.; Finkbeiner, T. Impact of carbonate content, rock texture, and roughness on fracture transmissivity and acid-etching patterns in carbonate rocks. *Rock Mech. Rock Eng.* **2024**, *57*, 6683–6699. [CrossRef]
9. Gou, B.; Li, X.; Guo, J.; Liu, W.; Zeng, J.; He, C.; Hu, L.; Ren, J.; Dai, Q. Effect of acid type on acid-etched fracture surface morphology and conductivity along the fracture. *Energy Fuels* **2023**, *37*, 3709–3722. [CrossRef]
10. Liu, F.; Ma, H.; Li, L.; Zhou, C.; Luo, Z.; Gao, X.; Wu, Y. Acid-etched fracture length and conductivity experiments with relayed large-scale rock plates. *J. Pet. Sci. Eng.* **2021**, *196*, 107978. [CrossRef]
11. Parandeh, M.; Dehkohneh, H.Z.; Soulgani, B.S. Experimental investigation of the acidizing effects on the mechanical properties of carbonated rocks. *Geoenergy Sci. Eng.* **2023**, *222*, 211447. [CrossRef]
12. Zhang, H.; Zhong, Y.; Zhang, J.; Zhang, Y.; Kuang, J.; Yang, B. Experimental research on deterioration of mechanical properties of carbonate rocks under acidified conditions. *J. Pet. Sci. Eng.* **2020**, *185*, 106612. [CrossRef]
13. Zhou, B.; Jin, Y.; Xiong, W.; Zhang, J.; Lai, J.; Fang, Q. Investigation on surface strength of acid fracture from scratch test. *J. Pet. Sci. Eng.* **2021**, *206*, 109017. [CrossRef]
14. Oliver, W.C.; Pharr, G.M. An improved technique for determining hardness and elastic modulus using load and displacement sensing indentation experiments. *J. Mater. Res.* **1992**, *7*, 1564–1583. [CrossRef]
15. Abdallah, Y.; Vandamme, M.; Chateau, C.; Garnier, D.; Jolivet, I.; Onaisi, A.; Richard, D.; Zandi, S.M. Linking elastic properties of various carbonate rocks to their microstructure by coupling nanoindentation and SEM-EDS. *Int. J. Rock Mech. Min. Sci.* **2023**, *170*, 105456. [CrossRef]
16. Feng, W.; Yang, C.; Tao, S.X.; Wang, C.Z.; Lu, Y.Y.; Zhang, L.F.; Zhou, F.J. Experimental study on the surface feature of acid-etched fractures in carbonate rocks. *Lithol. Reserv.* **2020**, *32*, 166–172. [CrossRef]

17. Chen, Y.S. Study on Fractal Characteristics of Acid Erosion Morphology and Reaction Kinetics Behavior of Carbonate Rocks. Master's Thesis, Southwest Petroleum University, Chengdu, China, 2018.
18. Dai, Y.F.; Hou, B. Correlation analysis between acid-etched fracture surface roughness and fracture conductivity in carbonate reservoir. *Fault-Block Oil Gas Field* **2023**, *30*, 672–677.
19. Deng, J.L. Control problems of grey systems. *Syst. Control Lett.* **1982**, *1*, 288–294. [CrossRef]

Disclaimer/Publisher's Note: The statements, opinions and data contained in all publications are solely those of the individual author(s) and contributor(s) and not of MDPI and/or the editor(s). MDPI and/or the editor(s) disclaim responsibility for any injury to people or property resulting from any ideas, methods, instructions or products referred to in the content.